Mitigating the Interfacial Degradation in Cathodes for High-Performance Oxide-Based Solid-State Lithium Batteries

Dawei Wang,[†] Qian Sun,[†] Jing Luo,[†] Jianneng Liang,[†] Yipeng Sun,[†] Ruying Li,[†] Keegan Adair,[†] Li Zhang,[‡] Rong Yang,[‡] Shigang Lu,[‡] Huan Huang,[§] and Xueliang Sun*,[†]

[†]Department of Mechanical and Materials Engineering, University of Western Ontario, London, Ontario N6A 5B9, Canada
[‡]China Automotive Battery Research Institute, Beijing 100088, China
[§]GLABAT Solid-State Battery Inc., London, Ontario N6G 4X8, Canada

S *Supporting Information*

ABSTRACT: Solid-state lithium batteries (SSLBs) are the promising next-generation energy storage systems because of their attractive advantages in terms of energy density and safety. However, the interfacial engineering and battery building are of huge challenges, especially for stiff oxide-based electrolytes. Herein, we construct SSLBs by a cosintering method using Li_3BO_3 as a sintering agent to bind the cathode materials $LiNi_{0.6}Mn_{0.2}Co_{0.2}O_2$ (NMC) and solid-state electrolytes $Li_{6.4}La_3Zr_{1.4}Ta_{0.6}O_{12}$. Small NMC primary particles are compared with large secondary particles

to study the effects on interfacial adhesion, mechanical retention, internal resistance evolution, and electrochemical performance. Our results reveal that the interfacial resistance decreases during charging and increases during discharging, resulting in an overall increase in the interfacial resistance after one cycle. The main reason is attributed to the microcracks induced by the volumetric changes of NMC during the electrochemical process. The mechanical degradations at the interfaces accumulated upon cycling can cause capacity decay and low Coulombic efficiency. The SSLB constructed from small NMC primary particles shows regulation of particle distribution, mitigation in local volumetric change, and alleviation in mechanical degradation at the interfaces, leading to smaller resistance change and better electrochemical performance. The findings shed lights on designing SSLBs with good mechanical retention and electrochemical performance.

KEYWORDS: solid-state lithium battery, interfacial degradation, microcrack, cosintering, size regulation, internal resistance
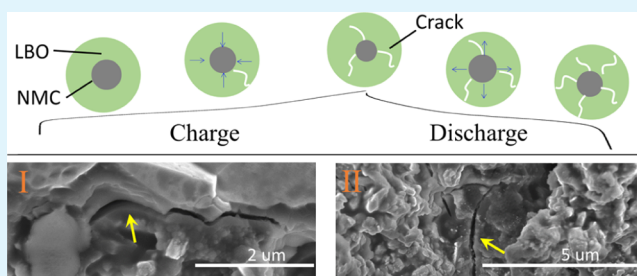
1. INTRODUCTION

Nowadays, lithium ion batteries (LIBs) have become the dominant energy storage systems for mobile electronics, electric vehicles, and smart grids because of their advantages in energy density over other systems.[1−3] However, conventional LIBs are reaching the ceiling of energy density based on the current electrode materials and cell designs. The organic liquid electrolytes used in the conventional LIBs are the key issues. First, the organic electrolytes have a narrow electrochemical window and are likely to be oxidized at high voltage.[4] The full capacities of high-voltage cathodes, such as spinel $LiNi_{0.5}Mn_{1.5}O_4$ and Ni-rich $Li[NiMnCo]O_2$, are thus limited.[5,6] Second, most organic liquid electrolytes are prone to cause Li dendrite formation when using Li metal as an anode, which has led to several serious accidents before the development of LIBs.[7] Furthermore, the flammable organic electrolytes may cause fire and even explosion upon internal short-circuit and thermal runaway.[8,9] Alternatively, inorganic solid-state electrolytes (SSEs) are attractive candidates to replace current liquid electrolytes because of their beneficial intrinsic properties.[10] Typically, a wide electrochemical window (with passivation) of SSEs can extend the working

voltage to enable high-capacity utilizations of high-voltage cathodes;[11−13] the high mechanical strength can help to alleviate Li dendrite growth and realize the application of Li metal anodes;[14,15] and the inflammable nature of SSEs can fundamentally improve the safety of solid-state lithium batteries (SSLBs).

Inorganic SSEs have attracted great research interest with their intrinsic advantages and have been developing rapidly since last 2 decades.[16−18] The maximum ionic conductivity can reach the order of 10^{-2} S cm^{-1} for sulfide SSEs (e.g., $Li_{10}GeP_2S_{12}$) and 10^{-3} to 10^{-4} S cm^{-1} for oxide SSEs (e.g. $Li_{6.5}La_3Zr_{1.5}Ta_{0.5}O_{12}$),[19−21] which have satisfied the basic conductivity requirement of SSLBs. Compared to the sulfide SSEs, oxide SSEs are more stable with ambient atmosphere and electrode materials,[22−24] making them more preferable for SSLBs from the standpoint of large-scale manufacturing. However, the interfacial engineering and fabrication of SSLBs are still challenging because of the stiffness of both
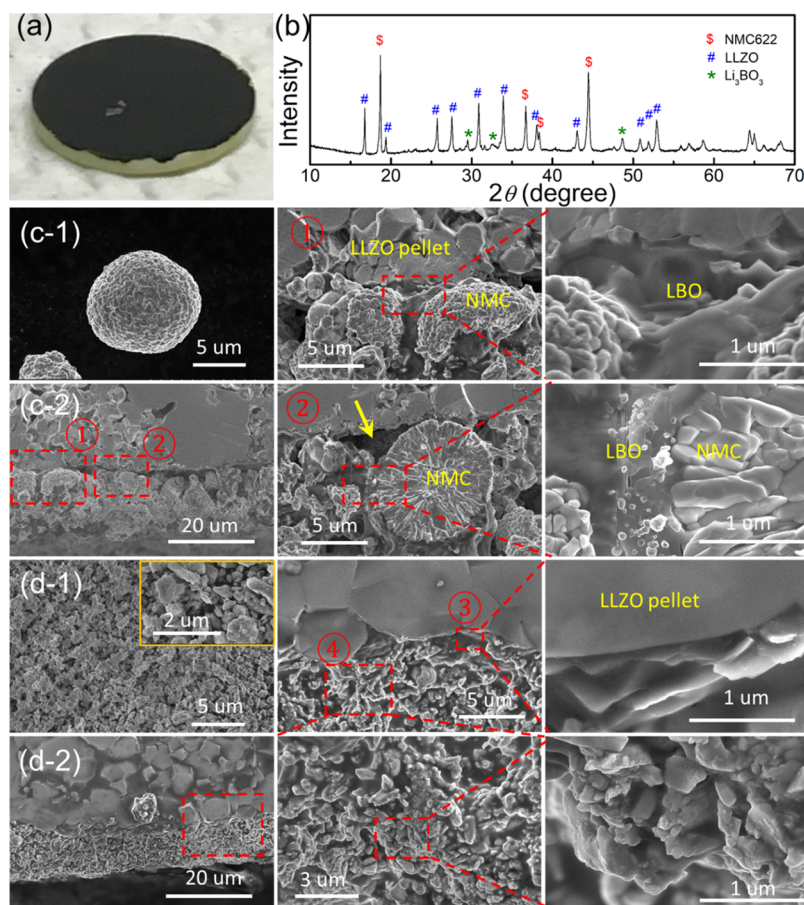
Figure 1. Morphology and crystalline structure of cathode/electrolyte composites. (a) Optical image of a cathode/electrolyte composite pellet. (b) XRD pattern of the cathode/electrolyte composite with small-NMC. The NMC, LLZO, and LBO peaks are labeled by $, #, and *, respectively. The XRD pattern of raw materials are shown in Figure S1. (c-1) Morphology of large-NMC and (c-2) cross-sectional SEM images of cathode/electrolyte composites composed of large-NMC. (d-1) Morphology of small-NMC and (d-2) cross-sectional SEM images of cathode/electrolyte composites composed of small-NMC.

cathode materials and SSEs.[14] Although 3D designs can quantitatively increase the contact area between the cathode materials and the SSEs, qualitative improvement of the interface is difficult to achieve. The resulting solid-state cathode exhibited a large interfacial resistance and a low specific capacity of 15 mA h g^{-1} even if operated at 95 °C.[25] Post heat treatment can qualitatively increase the interfacial binding by partial melting of SSEs; however, side reactions are usually accompanied and thus increase the interfacial resistance as a side effect.[26] One strategy is to lower the sintering temperature and shorten the dwell time by advanced sintering techniques, such as spark plasma sintering.[27] However, these advanced sintering techniques are very expensive and difficult to be popularized. Another more favorable strategy is called "cosintering" which is achieved by introducing a buffer layer between the cathode material and the SSE to prevent their direct contact and inter-reactions. In addition, introduction of a functional buffer layer can also enhance the interfacial dynamics.[28,29] By taking advantage of dissolution−precipitation of raw materials with the aid of a liquid solvent at low temperatures, cold sintering is favored over the hot calcination method for the development of SSLBs because of the ability to avoid thermal side reactions at high temperatures.[30,31] However, more demonstrations are needed before wide application of the cold sintering method can be achieved.

LiCoO$_2$ cathodes and garnet SSEs (e.g., Li$_7$La$_3$Zr$_2$O$_{12}$ with Al, Ta, and so forth doping) are common choices for SSLBs. However, direct calcination at 700 °C can cause interdiffusion of Al atoms and transformation of the surface Li$_{6.4}$La$_3$Zr$_{1.4}$Ta$_{0.6}$O$_{12}$ (LLZO) from highly conductive cubic phase to low conductive tetrahedral phase, leading to the deterioration of the electrochemical performance (~35 mA h g^{-1}, only 25% of practical capacity).[26] An oxide SSE Li$_3$BO$_3$ (LBO) with a low melting point of 700 °C was proposed as a sintering aid and buffer layer for the cosintering method.[32] Depending on the sintering properties and charge/discharge conditions, the SSLBs (based on the cathode of LiCoO$_2$) with LBO as a cosintering additive exhibited enhanced specific capacities ranging from 67 to 85 mA h g^{-1}.[33−36] Recently, Han et al. ingeniously designed the LiCoO$_2$/SSE interface by taking advantage of the reaction between Li$_2$CO$_3$ and LBO to form a higher conductive Li$_{3.3}$B$_{0.7}$C$_{0.3}$O$_3$ transition layer. The resulting composite cathode showed an improved specific capacity of 94 mA h g^{-1} at room temperature.[37] While the cosintering technique demonstrated feasibility results with the LiCoO$_2$ cathode, the specific capacity is expected to be further improved using high-capacity cathode materials such as Ni-rich Li[NiMnCo]O$_2$.[38,39] In addition, the opposite volumetric behaviors between LiCoO$_2$ and Li[NiMnCo]O$_2$ during the charge/discharge process can lead to different results and new insights for SSLB interfacial engineering.[40]
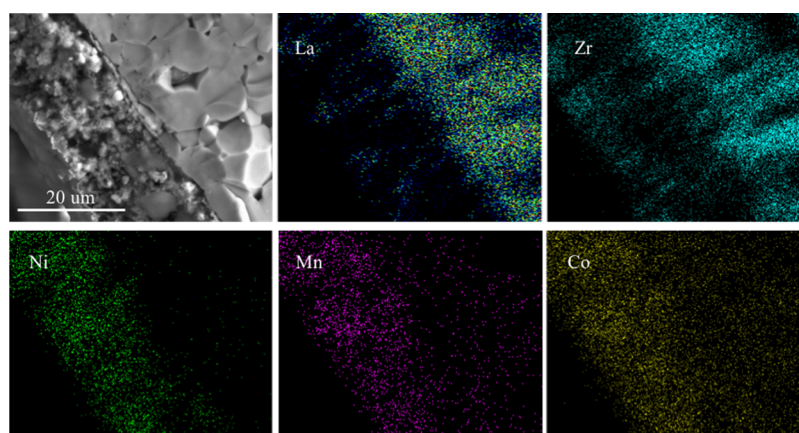
Figure 2. Elemental distribution of the electrode cross section of small-NMC.

Herein, we investigated SSLBs with high-capacity Li-Ni$_{0.6}$Mn$_{0.2}$Co$_{0.2}$O$_2$ (NMC) as the cathode, LLZO as the SSEs, and LBO as the sintering aid and buffer layer to achieve cosintering. The mechanical, electrical, and electrochemical behaviors of the particular SSLBs during the electrochemical process were studied. Our results revealed that the volume change of cathode materials during the charge/discharge process caused mechanical decay in SSLBs, typically present in the form of microcracks in the composite cathode. The mechanical degradation resulted in increasing interfacial resistance, which degraded the electrochemical performance of SSLBs. The SSLBs constructed with small NMC particles exhibited a better mechanical retention, a slower interfacial resistance increase, and a better electrochemical performance than those constructed with large NMC particles. Our findings shed light on the fundamental understanding of volume change, mechanical degradation, interface evolution, and electrochemical performance during the electrochemical process, aiming to build a better SSLB.

2. EXPERIMENTAL SECTION

2.1. Preparation of the Bilayer Cathode/Solid Electrolyte. The LLZO (CAS Shanghai, China) powder was pressed into pellets and calcined at 1200 °C for 12 h. The pellets were polished to a thickness of 0.5 mm with sand paper. The LBO was prepared from the raw materials of LiOH and H$_3$BO$_3$ by two-step calcination at 500 °C for 1 h and 600 °C for 2 h (Figure S1). NMC (MTI, Figure S1), LLZO powers, and LBO were mixed in a weight ratio of 58:30:12. No other conductive carbon was added in the cathode composite. The cathode composite was mixed with ethyl cellulose as a binder using a-terpineol as a solvent to prepare the electrode slurry. The slurry was then coated on the top surface of the LLZO pellet, and the solvent was removed by vacuum-drying at 60 °C overnight. The LLZO-supported composite cathode was cosintered at 700 °C for 1 h in air. For comparison, the secondary NMC particles were ground into primary particles for testing in SSLBs. The loading of cathode materials is about 1.5–2.0 mg. A thin layer of gold (200 nm) was sputtered on the top of the cathode using a sputter coater (MNT-JS1600) to improve the electronic contact between the cathode and current collector.

2.2. Morphology and Structure. The crystal structure of the as-prepared solid-state electrodes was characterized using X-ray powder diffraction. A Bruker X'Pert (Bruker, Germany) instrument with Cu Kα radiation was used for this purpose. A Hitachi S-4800 scanning electron microscope accompanied with an energy-dispersive X-ray scattering system was used to check the cross-sectional morphology and elemental distribution of samples.

2.3. Electrochemical Impedance Spectroscopy. Gold was sputtered on both surfaces of LLZO pellets as the current collector. Alternating current (ac) impedance measurements were undertaken to measure conductivity, using a Bilogic impedance analyzer with the frequency range of 1 to 10^5 Hz and an amplitude of 50 mV. The impedance evolution during the charge and discharge process of the SSLB was characterized in the frequency range of 1 to 10^5 Hz, and the amplitude is 50 mV. The impedance spectra were analyzed using ZView software.

2.4. Electrochemical Measurements. These composite cathodes were assembled into 2032-type coin cells in an argon-filled glovebox for electrochemical measurements, with a metallic lithium foil (MIT Crop.) as the counter electrode, and the gel electrolyte was inserted between the LLZO pellet and Li metal to improve the interfacial properties. The galvanostatic charge–discharge analysis was performed at 0.05 C (1 C = 115 mA h g^{-1}) using a battery cycler (Arbin Instrument, BT-2400) in constant current mode in the voltage range of 3.0–4.2 V at room temperature.

3. RESULTS AND DISCUSSION

Garnet-type SSE LLZO powder was achieved and sintered into pellets. The LLZO showed a pure cubic phase with an ionic conductivity of 4 × 10^{-4} S cm^{-1} (Figures S1 and S2), comparable to the value reported in the literatures.[19−21] A bilayer cathode/SSE composite pellet was composed of a cathode layer of NMC, LLZO, and LBO with an SSE layer of pure LLZO. The composite pellet was prepared by cosintering at 700 °C (Figure 1a). X-ray diffraction (XRD) patterns after cosintering confirmed the thermal stability of NMC, LLZO, and LBO as no impurity peak was observed and the retaining of their favorable crystalline structures (Figure 1b).

Figure 1c,d compares the scanning electron microscopic (SEM) morphologies of the as-prepared cathode/SSE composite pellets with large or small NMC particles. As shown in Figure 1c-1, the large NMC particles were actually agglomerates of numerous small primary particles, resulting in secondary particles ranging from 5 to 10 μm. After cosintering, the NMC and LLZO generally maintained their particle-like morphologies, whereas LBO melted and filled in the gaps between the particles (Figure 1c-2). The expected role of LBO was to bind the NMC and the LLZO particles as well as the SSE layer with an intimate interface to ensure good interfacial contact (Figure 1c-2, area ①). However, in the presence of large NMC agglomerates, some gaps were too large to be filled up, leaving the NMC surface partially uncovered (Figure 1c-2, area ②). Notably, the uncovered surface and the NMC primary particles buried inside the agglomerates were not accessible to
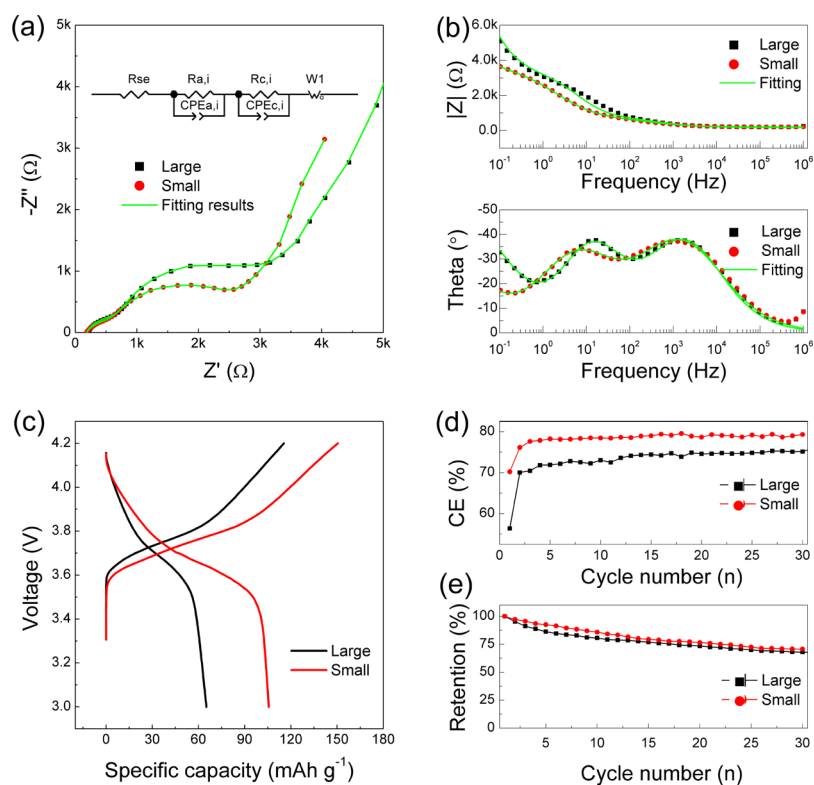
Figure 3. Electrical and electrochemical properties of SSLBs. (a) Nyquist plot, (b) Bode plot, (c) 1st cycle charge−discharge profiles, corresponding (d) CE, and (e) retention of SSLBs.

fast Li$^+$ conduction. To address this problem, primary NMC particles of ~500 nm were retrieved by hand-milling the agglomerates (Figure 1d-1). For brevity, the small NMC primary particles are referred as small-NMC and the large NMC agglomerates are referred as large-NMC. Replacing the large-NMC with small-NMC, the resulting cosintered composite cathode showed a much denser arrangement (Figure 1d-2), with the small-NMC and LLZO particles embedded homogeneously in the LBO matrix (area ③, ④). All the small-NMC particles, LLZO particles, and the joint to the SSE layer were fully bound by the malleable LBO. The continuous cross-sectional morphology indicated good interfacial contacts.

Figure 2 shows the elemental distribution of the cross section of small-NMC. The elements La and Zr were rich in the LLZO layer and less in the cathode composite, as the concentration of LLZO in the cathode composite is much lower than that in the LLZO layer. Ni, Mn, and Co were homogeneously located in the cathode composite. As a light element, B is not sensitive to X-ray, so the B mapping was not shown here. Both SEM and elemental mappings indicated a homogeneous distribution of the NMC cathode and the LLZO SSE amid the LBO SSE matrix in the cathode composite.

Electrochemical impedance spectroscopy (EIS) spectra were collected to study the electrical properties of SSLBs using the NMC-LLZO-LBO/LLZO cathode/SSE composite pellets (Figure 3a,b). A gel polymer electrolyte (GPE) was placed in between the composite pellet (the SSE layer side) and the Li metal anode to enhance wetting. The spectra typically consisted of an intercept at high frequency, two semicircles at middle frequency, and a tail at low frequency. The intercept at 10^6 to 10^4 Hz with a value of ~200 Ω represented the total resistance of the LLZO in the cathode/SSE composite pellets

and GPE. The first semicircle at 10^4 to 10^3 Hz with a value of ~400 Ω was attributed to the interfacial resistance of the Li metal/GPE interface as well as the GPE/LLZO interface (see the EIS spectra for the Li|GPE|LLZO|GPE|Li symmetric cell in Figure S3). The second semicircle at 10^1 to 10^2 Hz represented the interfacial charge transfer resistance at the cathode interface. The composite cathode constructed from large-NMC shows a larger interfacial resistance (2500 Ω) than that constructed from small-NMC (2300 Ω). The significant decrease in the cathode interfacial resistance, indicating a better interfacial contact with small-NMC, was consistent with the SEM results (Figure 1c,d). The tail at 10^{-1} to 10^1 Hz represented the Li$^+$ diffusion in the NMC material.

The electrochemical performance of SSLBs with large- or small-NMC is shown in Figure 3c. The small-NMC cell delivered a much higher initial charge/discharge capacity of 160 and 106 mA h g^{-1} than the large-NMC cell with 118 mA h g^{-1} initial charge and 65 mA h g^{-1} discharge capacity at 0.05 C at room temperature. On the one hand, the effective NMC/LBO and LBO/LLZO interfaces in the small-NMC cell ensured the NMC utilization; on the other hand, the small-NMC also possessed a much more efficient Li$^+$ diffusion path than the large-NMC within the particle. Considering the radius of particles, the Li$^+$ diffusion length in the small-NMC is already roughly 20 times shorter than that in the large-NMC, not to mention that Li$^+$ has to hop through the grain boundaries between the NMC primary particles within the large-NMC. Nevertheless, the discharge capacity of the small-NMC cell is comparable to that of the reported LiCoO$_2$-based SSLBs.[37] Even though the small-NMC cell experienced deeper charge and discharge, the small-NMC cell showed a higher Coulombic efficiency (CE) and better capacity retention over 30 cycles (Figure 3d), presumably due to Li$^+$ trapping inside
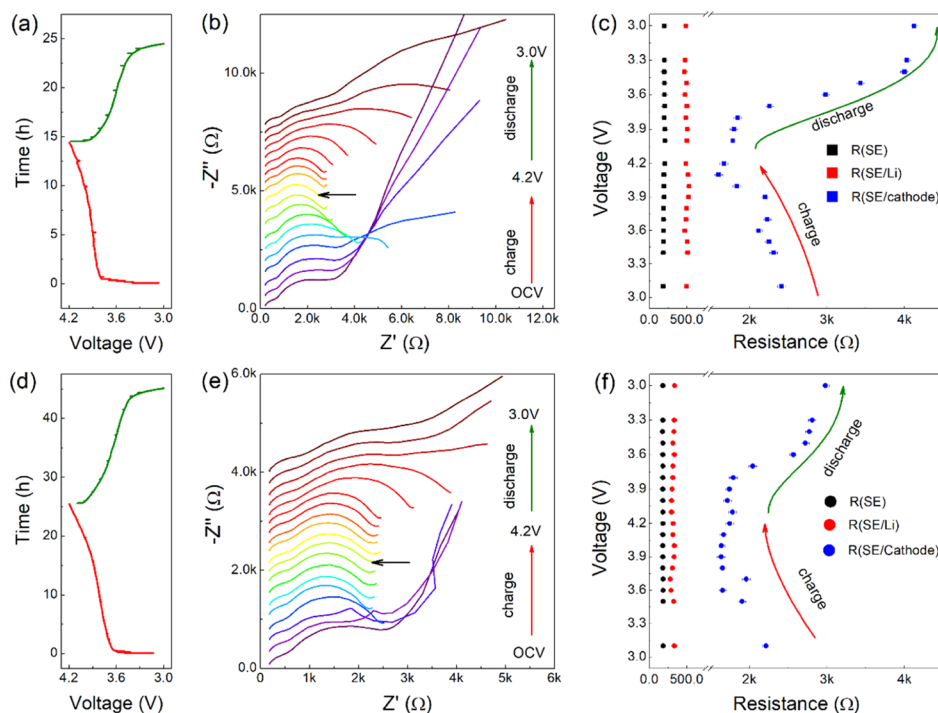
Figure 4. Impedance evolution of SSLBs during the charge and discharge process. (a) Charge−discharge profile, (b) impedance evolution during the charge−discharge process, (c) associated resistance extracted from the fitted EIS spectra of SSLBs constructed with large-NMC, (d) charge−discharge profile, (e) impedance evolution during the charge−discharge process, and (f) associated resistance extracted from the fitted EIS spectra of SSLBs constructed with small-NMC.
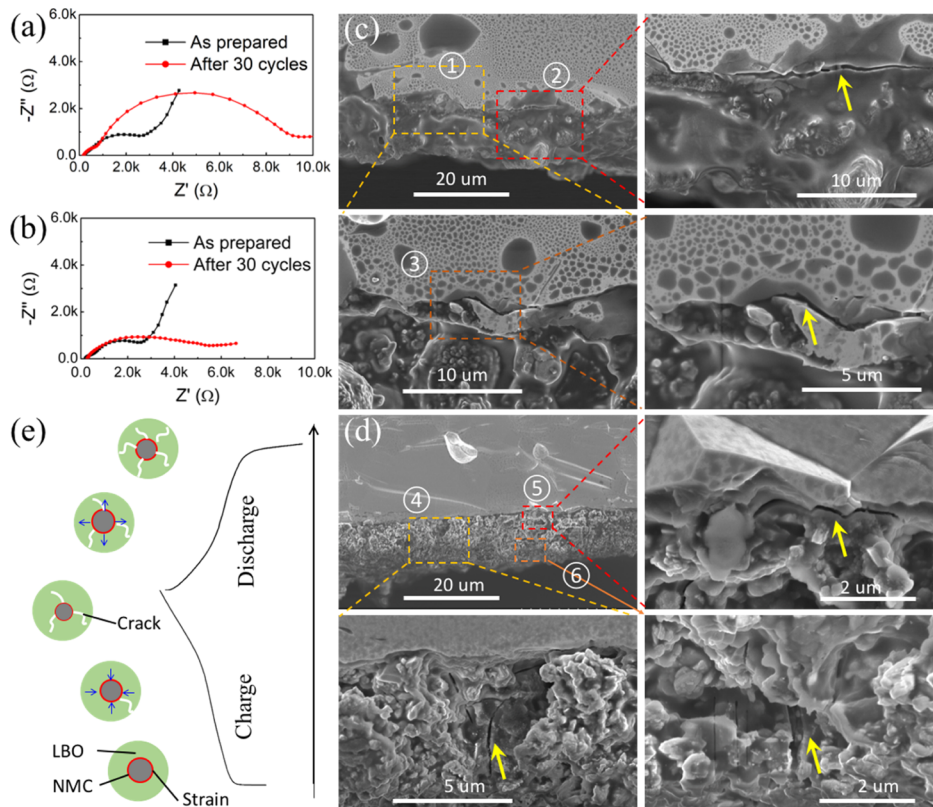

Figure 5. Impedance, morphology of composite cathode/electrolyte after cycling and schematic of mechanical degradation. (a,b) EIS spectra of SSLBs constructed with large-NMC and small-NMC at the initial state and after 30 cycles. (c) Composite cathode constructed with large-NMC after 30 cycles. (d) Composite cathode constructed with small-NMC after 30 cycles. (e) Schematic of the initial state and mechanical degradation in the cathode composite. Cracking occurs at within the LBO and corresponding interfaces with NMC and LLZO. The blue line represents the volume change during the charge−discharge process.

the large-NMC. However, the failure mode for the relatively low CEs (55% for the large-NMC cell and 70% for the small-NMC cell) and the capacity deteriorations should be better understood to design practical NMC-based SSLBs.

In operando EIS analysis was performed to understand the impedance evolutions of SSLBs containing large- or small-NMC during charging and discharging. Figure 4a,d is the corresponding charge−discharge voltage profiles. The EIS spectra during charge and discharge (Figure 4b,e) generally maintained a shape similar to that of the EIS spectra for the as-prepared cells (Figure 3a). Overall, the total resistance decreased during charging and increased during discharging. The fully recharged impedance after the 1st cycle was higher than the initial value. The shape of the tail at low frequency also varied upon charge and discharge, indicating different Li$^+$ diffusion behaviors within the bulk NMC at different states of charge (Figure 4b,e). The EIS spectra were fitted using the model of $R_{SSE}(R_{a,i}CPE_{a,i})(R_{c,i}CPE_{c,i})W_o$. The fitting results of the three key components including the bulk electrolyte resistance (R_{SSE}), the anode interfacial resistance ($R_{a,i}$), and the cathode interfacial resistance ($R_{c,i}$) were summarized in Figure 4c,f. Because the bulk LLZO is stable and same in both cells, it is not surprising that R_{SSE} remains unchanged and highly similar in values for both cells. Upon charge and discharge, the stable values of $R_{a,i}$ indicated stable interfaces of LLZO/GPE and GPE/Li. After all, the major difference occurred at the cathode side. The large-NMC cell exhibited large fluctuations in $R_{c,i}$ over cycling, whereas the small-NMC cell maintained relatively stable $R_{c,i}$. For the large-NMC cell, $R_{c,i}$ decreased from 2500 to 1600 Ω (36% difference) upon charging and then increased to 4100 Ω (156% difference) during the discharge process. In contrast, $R_{c,i}$ of the small-NMC cell varied from 2300 to 1700 Ω (26% decrease) during charging and returned to 2900 Ω (71% increase) during discharging. The small-NMC cell experienced a much lower overall $R_{c,i}$ increase (26%) than the large-NMC cell (64%) after the 1st cycle. This finding is consistent with the electrochemical performance that the small-NMC cell possessed higher CE than the large-NMC cell.

As the increase in resistance accumulated over cycles, the total resistance of the large-NMC cell increased rapidly to 9500 Ω after 30 cycles, doubling the resistance of the small-NMC cell (Figure 5a,b). Correspondingly, the small-NMC cell showed better capacity retention than the large-NMC cell upon cycling (Figure 3b). To understand the cause of degradation, the two cells were disassembled and characterized by SEM. As shown in Figure 5c,d, micrometer-sized cracks formed across the joint between the large-NMC cathode layer and the SSE layer, while the small-NMC cell formed vertical cracks within the cathode layer. These cracks were presumably caused by the volumetric change of the NMC particles during charging and discharging.[41] Typically, NMC shrinks during charging and expands during discharging (Figure S4).[40] Figure 5e schematically illustrates the mechanical cracking process upon one cycle. Although the LBO reshaped during the cosintering process to fill in the gaps between the NMC and the LLZO particles in the cathode layer, the LBO remained solid after fabrication and served little buffer to volume change. Because the large-NMC was actually secondary particles building from small-NMC, the large-NMC had to bear the accumulated volume expansion or shrinkage of the constituent small-NMC particles. Assuming the same depth of charge/discharge and 2% volume change during the process (as

depicted in Figure S4d), a 10 nm volume change would be created surrounding a small-NMC particle versus a much larger volume change around a large-NMC particle (should be larger than 10 nm of a single primary NMC particle but smaller than 200 nm because of the porosity of secondary NMC particles). The serious volumetric change of large-NMC led to the detachment of the cathode layer off the SSE layer, causing a significant barrier of Li$^+$ conduction. In contrast, the small-NMC managed to mitigate the local volume change within the cathode layer. Even though vertical cracks in the cathode layer could cause an increase in the internal resistance, Li$^+$ conduction across the cell was maintained.

As unfavorable electrochemical side reactions usually produce insulating side products leading to an increase in the interfacial resistance, the observed increasing impedance could have been mistakenly attributed to interfacial instabilities. XRD patterns collected at different states of charge indicated that the cathode composites are electrochemically stable during charging and discharging, at least, within the sensitivity of the XRD technique (Figure S4). Furthermore, even if NMC is unstable against LBO or LLZO, the small-NMC cell should have suffered from more severe side reactions than the large-NMC cell because of larger contacting areas. However, the empirically smaller resistance for the small-NMC cell is contradictory to this assumption. In addition, electrochemical oxidations tend to occur at high voltages, which means impedance is more likely to increase during charging rather than discharging. However, not only the in operando EIS study showed an opposite trend but also the small-NMC cell presented less fluctuation in $R_{c,i}$. This again cannot be explained by the interfacial side reactions during the charge−discharge process. Therefore, even if NMC reacts with LBO or LLZO, interfacial side reactions were not the major cause for the severe impedance increase and performance deteriorations.

4. CONCLUSIONS

The bilayer cathode/SSE composite was fabricated by cosintering NMC, LBO, and LLZO. The SSLB constructed from small-NMC primary particles achieved a much higher capacity of 106 mA h g^{-1} than the ones constructed using large NMC secondary particles. The improvements were attributed to the better interfacial properties as well as the shorter Li$^+$ diffusion path within the small-NMC. However, mechanical degradation in the form of microcracks in the cathode composite, primarily within the LBO and at their interfaces between NMC and LLZO, was found to be the key reason for the cathode interfacial degradation and capacity deterioration. Although the LBO melted to fill in the gaps between the NMC and the LLZO particles during cosintering, the LBO and all other components in the SSLB remained stiff during cycling. Using small NMC primary particles rather than large secondary particles can help to alleviate the mechanical degradation by mitigating the local volume change, subsequently improving CE and capacity retention. This work highlights the correlations among volume change of active materials, mechanical degradation, resistance evolution, and electrochemical performance in SSLBs. Developing new designs such as mitigating the local volume change and incorporating a soft buffer layer would be an important future direction.

■ ASSOCIATED CONTENT

ⓢ Supporting Information

The Supporting Information is available free of charge on the ACS Publications website at DOI: 10.1021/acsami.8b17881.

XRD patterns of raw materials; EIS spectra of LLZO pellets; EIS spectra of symmetric Li|GPE|LLZO|GPE|Li cell; and ex situ XRD patterns of the cathode composite during charge and discharge (PDF)

■ AUTHOR INFORMATION

Corresponding Author

*E-mail: xsun9@uwo.ca.

ORCID ⓘ

Xueliang Sun: 0000-0003-2881-8237

Author Contributions

X.S. conceived the concept and initiated the project. D.W., Q.S., J.L., J.L., Y.S., R.L., and K.A. conducted the measurements and analyzed the data. L.Z., R.Y., S.L., H.H. assisted with data analysis and figure preparation. D.W., J.L., and X.S. wrote the paper. All authors were involved in revising the manuscript.

Notes

The authors declare no competing financial interest.

■ ACKNOWLEDGMENTS

■ ABBREVIATIONS

LIB, lithium ion battery
SSLB, solid-state lithium battery
SSEs, solid-state electrolyte
NMC, $LiNi_{0.6}Mn_{0.2}Co_{0.2}O_2$
LLZO, $Li_{6.4}La_3Zr_{1.4}Ta_{0.6}O_{12}$
LBO, Li_3BO_3
GPE, gel polymer electrolyte
CE, Coulombic efficiency
XRD, X-ray diffraction
EIS, electrochemical impedance spectroscopy

■ REFERENCES

(1) Tarascon, J.-M.; Armand, M. Issues and Challenges Facing Rechargeable Lithium Batteries. *Nature* **2001**, *414*, 359−367.

(2) Armand, M.; Tarascon, J.-M. Building Better Batteries. *Nature* **2008**, *451*, 652−657.

(3) Choi, J. W.; Aurbach, D. Promise and Reality of Post-Lithium-Ion Batteries with High Energy Densities. *Nat. Rev. Mater.* **2016**, *1*, 16013.

(4) Goodenough, J. B.; Kim, Y. Challenges for Rechargeable Li Batteries. *Chem. Mater.* **2010**, *22*, 587−603.

(5) Xiao, B.; Liu, H.; Liu, J.; Sun, Q.; Wang, B.; Kaliyappan, K.; Zhao, Y.; Banis, M. N.; Liu, Y.; Li, R.; Sham, T.-K.; Botton, G. A.; Cai, M.; Sun, X. Nanoscale Manipulation of Spinel Lithium Nickel Manganese Oxide Surface by Multisite Ti Occupation as High-Performance Cathode. *Adv. Mater.* **2017**, *29*, 1703764.

(6) Wang, D.; Kou, R.; Ren, Y.; Sun, C.-J.; Zhao, H.; Zhang, M.-J.; Li, Y.; Huq, A.; Ko, J. Y. P.; Pan, F.; Sun, Y.-K.; Yang, Y.; Amine, K.; Bai, J.; Chen, Z.; Wang, F. Synthetic Control of Kinetic Reaction Pathway and Cationic Ordering in High-Ni Layered Oxide Cathodes. *Adv. Mater.* **2017**, *29*, 1606715.

(7) Yoshino, A. The Birth of the Lithium-Ion Battery. *Angew. Chem., Int. Ed.* **2012**, *51*, 5798−5800.

(8) Wang, Q.; Ping, P.; Zhao, X.; Chu, G.; Sun, J.; Chen, C. Thermal Runaway Caused Fire and Explosion of Lithium Ion Battery. *J. Power Sources* **2012**, *208*, 210−224.

(9) Bandhauer, T. M.; Garimella, S.; Fuller, T. F. A Critical Review of Thermal Issues in Lithium-Ion Batteries. *J. Electrochem. Soc.* **2011**, *158*, R1−R25.

(10) Liu, K.; Liu, Y.; Lin, D.; Pei, A.; Cui, Y. Materials for Lithium-Ion Battery Safety. *Sci. Adv.* **2018**, *4*, No. eaas9820.

(11) Thompson, T.; Yu, S.; Williams, L.; Schmidt, R. D.; Garcia-Mendez, R.; Wolfenstine, J.; Allen, J. L.; Kioupakis, E.; Siegel, D. J.; Sakamoto, J. Electrochemical Window of the Li-Ion Solid Electrolyte $Li_7La_3Zr_2O_{12}$. *ACS Energy Lett.* **2017**, *2*, 462−468.

(12) Richards, W. D.; Miara, L. J.; Wang, Y.; Kim, J. C.; Ceder, G. Interface Stability in Solid-State Batteries. *Chem. Mater.* **2015**, *28*, 266−273.

(13) Oh, G.; Hirayama, M.; Kwon, O.; Suzuki, K.; Kanno, R. Bulk-Type All Solid-State Batteries with 5V Class $LiNi_{0.5}Mn_{1.5}O_4$ Cathode and $Li_{10}GeP_2S_{12}$ Solid Electrolyte. *Chem. Mater.* **2016**, *28*, 2634−2640.

(14) Yu, S.; Schmidt, R. D.; Garcia-Mendez, R.; Herbert, E.; Dudney, N. J.; Wolfenstine, J. B.; Sakamoto, J.; Siegel, D. J. Elastic Properties of the Solid Electrolyte $Li_7La_3Zr_2O_{12}$ (LLZO). *Chem. Mater.* **2015**, *28*, 197−206.

(15) Monroe, C.; Newman, J. The Impact of Elastic Deformation on Deposition Kinetics at Lithium/Polymer Interfaces. *J. Electrochem. Soc.* **2005**, *152*, A396−A404.

(16) Thangadurai, V.; Narayanan, S.; Pinzaru, D. Garnet-Type Solid-State Fast Li Ion Conductors for Li Batteries: Critical Review. *Chem. Soc. Rev.* **2014**, *43*, 4714−4727.

(17) Zhang, Z.; Shao, Y.; Lotsch, B.; Hu, Y.-S.; Li, H.; Janek, J.; Nazar, L. F.; Nan, C.-W.; Maier, J.; Armand, M.; Chen, L. New Horizons for Inorganic Solid State Ion Conductors. *Energy Environ. Sci.* **2018**, *11*, 1945−1976.

(18) Fan, L.; Wei, S.; Li, S.; Li, Q.; Lu, Y. Recent Progress of the Solid-State Electrolytes for High-Energy Metal-Based Batteries. *Adv. Energy Mater.* **2018**, *8*, 1702657.

(19) Kamaya, N.; Homma, K.; Yamakawa, Y.; Hirayama, M.; Kanno, R.; Yonemura, M.; Kamiyama, T.; Kato, Y.; Hama, S.; Kawamoto, K.; Mitsui, A. A Lithium Superionic Conductor. *Nat. Mater.* **2011**, *10*, 682−686.

(20) Wang, D.; Zhong, G.; Pang, W. K.; Guo, Z.; Li, Y.; McDonald, M. J.; Fu, R.; Mi, J.-X.; Yang, Y. Toward Understanding the Lithium Transport Mechanism in Garnet-Type Solid Electrolytes: Li⁺ Ion Exchanges and Their Mobility at Octahedral/Tetrahedral Sites. *Chem. Mater.* **2015**, *27*, 6650−6659.

(21) Wang, D.; Zhong, G.; Dolotko, O.; Li, Y.; McDonald, M. J.; Mi, J.; Fu, R.; Yang, Y. The Synergistic Effects of Al and Te on the Structure and Li⁺-Mobility of Garnet-Type Solid Electrolytes. *J. Mater. Chem. A* **2014**, *2*, 20271−20279.

(22) Miara, L. J.; Richards, W. D.; Wang, Y. E.; Ceder, G. First-Principles Studies on Cation Dopants and Electrolyte|Cathode Interphases for Lithium Garnets. *Chem. Mater.* **2015**, *27*, 4040−4047.

(23) Zhu, Y.; He, X.; Mo, Y. First Principles Study on Electrochemical and Chemical Stability of Solid Electrolyte-Electrode Interfaces in All-Solid-State Li-Ion Batteries. *J. Mater. Chem. A* **2016**, *4*, 3253−3266.

(24) Tian, Y.; Shi, T.; Richards, W. D.; Li, J.; Kim, J. C.; Bo, S.-H.; Ceder, G. Compatibility Issues Between Electrodes and Electrolytes in Solid-State Batteries. *Energy Environ. Sci.* **2017**, *10*, 1150−1166.

(25) van den Broek, J.; Afyon, S.; Rupp, J. L. M. Interface-Engineered All-Solid-State Li-Ion Batteries Based on Garnet-Type Fast Li⁺ Conductors. *Adv. Energy Mater.* **2016**, *6*, 1600736.

(26) Park, K.; Yu, B.-C.; Jung, J.-W.; Li, Y.; Zhou, W.; Gao, H.; Son, S.; Goodenough, J. B. Electrochemical Nature of the Cathode Interface for a Solid-State Lithium-Ion Battery: Interface Between $LiCoO_2$ and Garnet-$Li_7La_3Zr_2O_{12}$. *Chem. Mater.* **2016**, *28*, 8051−8059.

(27) Woo, S. P.; Lee, S. H.; Yoon, Y. S. Characterization of LiCoO$_2$/Multiwall Carbon Nanotubes with Garnet-Type Electrolyte Fabricated by Spark Plasma Sintering for Bulk-Type All-Solid-State Batteries. *Composites, Part B* **2017**, *124*, 242−249.

(28) Liang, J.-Y.; Zeng, X.-X.; Zhang, X.-D.; Wang, P.-F.; Ma, J.-Y.; Yin, Y.-X.; Wu, X.-W.; Guo, Y.-G.; Wan, L.-J. Mitigating Interfacial Potential Drop of Cathode-Solid Electrolyte via Ionic Conductor Layer to Enhance Interface Dynamics for Solid Batteries. *J. Am. Chem. Soc.* **2018**, *140*, 6767−6770.

(29) Wang, L.-P.; Zhang, X.-D.; Wang, T.-S.; Yin, Y.-X.; Shi, J.-L.; Wang, C.-R.; Guo, Y.-G. Ameliorating the Interfacial Problems of Cathode and Solid-State Electrolytes by Interface Modification of Functional Polymers. *Adv. Energy Mater.* **2018**, *8*, 1801528.

(30) Guo, J.; Guo, H.; Baker, A. L.; Lanagan, M. T.; Kupp, E. R.; Messing, G. L.; Randall, C. A. Cold sintering: A Paradigm Shift for Processing and Integration of Ceramics. *Angew. Chem., Int. Ed.* **2016**, *55*, 11457−11461.

(31) Liu, Y.; Sun, Q.; Wang, D.; Adair, K.; Liang, J.; Sun, X. Development of the Cold Sintering Process and Its Application in Solid-State Lithium Batteries. *J. Power Sources* **2018**, *393*, 193−203.

(32) Tadanaga, K.; Takano, R.; Ichinose, T.; Mori, S.; Hayashi, A.; Tatsumisago, M. Low Temperature Synthesis of Highly Ion Conductive Li$_7$La$_3$Zr$_2$O$_{12}$-Li$_3$BO$_3$ Composites. *Electrochem. Commun.* **2013**, *33*, 51−54.

(33) Ohta, S.; Komagata, S.; Seki, J.; Saeki, T.; Morishita, S.; Asaoka, T. All-Solid-State Lithium Ion Battery Using Garnet-Type Oxide and Li$_3$BO$_3$ Solid Electrolytes Fabricated by Screen-Printing. *J. Power Sources* **2013**, *238*, 53−56.

(34) Ohta, S.; Seki, J.; Yagi, Y.; Kihira, Y.; Tani, T.; Asaoka, T. Co-Sinterable Lithium Garnet-Type Oxide Electrolyte with Cathode for All-Solid-State Lithium Ion Battery. *J. Power Sources* **2014**, *265*, 40−44.

(35) Shoji, M.; Munakata, H.; Kanamura, K. Fabrication of All-Solid-State Lithium-Ion Cells Using Three-Dimensionally Structured Solid Electrolyte Li$_7$La$_3$Zr$_2$O$_{12}$ Pellets. *Front. Energy Res.* **2016**, *4*, 32.

(36) Liu, T.; Ren, Y.; Shen, Y.; Zhao, S.-X.; Lin, Y.; Nan, C.-W. Achieving High Capacity in Bulk-Type Solid-State Lithium Ion Battery Based on Li$_{6.75}$La$_3$Zr$_{1.75}$Ta$_{0.25}$O$_{12}$ Electrolyte: Interfacial Resistance. *J. Power Sources* **2016**, *324*, 349−357.

(37) Han, F.; Yue, J.; Chen, C.; Zhao, N.; Fan, X.; Ma, Z.; Gao, T.; Wang, F.; Guo, X.; Wang, C. Interphase Engineering Enabled All-Ceramic Lithium Battery. *Joule* **2018**, *2*, 497−508.

(38) Liu, W.; Oh, P.; Liu, X.; Lee, M.-J.; Cho, W.; Chae, S.; Kim, Y.; Cho, J. Nickel-Rich Layered Lithium Transition-Metal Oxide for High-Energy Lithium-Ion Batteries. *Angew. Chem., Int. Ed.* **2015**, *54*, 4440−4457.

(39) Manthiram, A.; Song, B.; Li, W. A Perspective on Nickel-Rich Layered Oxide Cathodes for Lithium-Ion Batteries. *Energy Storage Mater.* **2017**, *6*, 125−139.

(40) Koerver, R.; Zhang, W.; de Biasi, L.; Schweidler, S.; Kondrakov, A. O.; Kolling, S.; Brezesinski, T.; Hartmann, P.; Zeier, W. G.; Janek, J. Chemo-mechanical expansion of lithium electrode materials - on the route to mechanically optimized all-solid-state batteries. *Energy Environ. Sci.* **2018**, *11*, 2142−2158.

(41) Liu, T.; Zhang, Y.; Chen, R.; Zhao, S.-X.; Lin, Y.; Nan, C.-W.; Shen, Y. Non-Successive Degradation in Bulk-Type All-Solid-State Lithium Battery with Rigid Interfacial Contact. *Electrochem. Commun.* **2017**, *79*, 1−4.